metals

MDPI

Article

Microstructures and Hardening Mechanisms of a 316L Stainless Steel/Inconel 718 Interface Additively Manufactured by Multi-Material Selective Laser Melting

Shahir Mohd Yusuf [1], Nurainaa Mazlan [1], Nur Hidayah Musa [1], Xiao Zhao [2], Ying Chen [3], Shoufeng Yang [4], Nur Azmah Nordin [1], Saiful Amri Mazlan [1] and Nong Gao [5,*]

1 Engineering Materials and Structures (eMast) iKohza, Malaysia-Japan International Institute of Technology (MJIIT), Universiti Teknologi Malaysia, Jalan Sultan Yahya Petra, Kuala Lumpur 54100, Malaysia
2 Aeronautical and Astronautical Department Southampton Boldrewood Innovation Campus, University of Southampton, Southampton SO16 7QF, UK
3 Fujian Provincial Key Laboratory of Functional Materials and Applications, Xiamen University of Technology, Xiamen 361024, China
4 Production Engineering, Machine Design and Automation Section, Department of Mechanical Engineering, Katholieke Universiteit Leuven (KU Leuven), 3001 Leuven, Belgium
5 Materials Research Group, Faculty of Engineering and Physical Sciences, University of Southampton, Southampton SO17 1BJ, UK
* Correspondence: n.gao@soton.ac.uk; Tel.: +44-(0)23-80593396

Abstract: For the first time, the interfacial microstructures and hardening mechanisms of a multi-material (MM) 316L stainless steel/Inconel 718 (316L SS/IN 718) interface fabricated by a novel multi-material selective laser melting (MM SLM) additive manufacturing (AM) system have been investigated in this study. MM 316L SS/IN 718 parts were successfully built with high densification levels (>99%) and low porosity content (average: ~0.81%). Microscopy analysis indicates that the interfacial microstructures are characterised by dense dislocation tangling networks, NbC and TiC, and very small amounts of Laves phase (<2 wt. %). In addition, equiaxed grains (average: 45 ± 3 µm) are attained in the interfacial region, whereas both individual IN 718 and 316L SS regions exhibit show columnar grains with average sizes of 55 ± 5 µm and 85 ± 3 µm, respectively. Vickers microhardness (HV) and nanoindentation measurements exhibit that the hardness values of the interfacial region are between those of the individual material regions. A strengthening model is built to assess the contribution of intrinsic strength, solid solution, precipitations, dislocations, and grain boundaries to the overall interfacial hardness of the as-built MM alloy.

Keywords: interfacial microstructures; hardening mechanisms; multi-material selective laser melting

Citation: Mohd Yusuf, S.; Mazlan, N.; Musa, N.H.; Zhao, X.; Chen, Y.; Yang, S.; Nordin, N.A.; Mazlan, S.A.; Gao, N. Microstructures and Hardening Mechanisms of a 316L Stainless Steel/Inconel 718 Interface Additively Manufactured by Multi-Material Selective Laser Melting. *Metals* **2023**, *13*, 400. https://doi.org/10.3390/met13020400

Academic Editors: Yongho Sohn and Le Zhou

Received: 6 January 2023
Revised: 4 February 2023
Accepted: 14 February 2023
Published: 15 February 2023

1. Introduction

High energy density fusion welding (HEDFW) techniques such as laser beam welding (LBW) and electron beam welding (EBW) and non-fusion welding (NFW) techniques such as friction stir welding (FSW) have been conventionally applied to join two or more dissimilar metals/alloys to obtain the combined favourable properties of the multiple materials within a single welded component, e.g., for aerospace, automotive, and nuclear reactor applications. Compared to low energy density fusion welding (LEDFW) processes, e.g., oxyfuel welding and arc welding, HEFW and NFW processes are able to yield high-quality welded joints and diffusion bonded regions and avoid problems that are associated with the use of filler metals in arc fusion welding [1]. For example, precipitates, intermetallics, and distortion are commonly formed at the interface of LEDFW weldments and often result in cracks and porosity, which deteriorates the strength and durability of the welded joints [1].

Although HEDFW and NFW processes can join two different metallic materials together, machining or forming processing may be needed to make them into the desired part geometry, resulting in increased time, cost, and material waste. Recently, advancements in metal additive manufacturing (AM) technologies have enabled the direct incorporation of multiple metal/alloy feedstock materials in a single machine operation, particularly via powder bed fusion (PBF) or directed energy deposition (DED) techniques that utilise a laser or electron beam as the heat source to consolidate the raw multi-material into a single complete 3D component, so-called multi-material AM (MMAM) [2]. Therefore, the MMAM-bonded interfacial region (joint between two materials) exhibits typical microstructural features such as the fusion zone (FZ), heat affected zone (HAZ), and unmixed zone (UZ), but it is often characterised by fine microstructures and grain sizes that usually yield high mechanical strength compared to traditionally welded joints [2,3]. Thus, MMAM offers the advantage of manufacturing two different materials simultaneously and is capable of producing complex shapes and intricate features. In addition, MMAM can shorten processing time, reduce material waste, and lower the associated manufacturing costs, with potentially enhanced mechanical properties when compared to conventional welding techniques [3].

Selective laser melting (SLM) is one of the most widely used metal AM techniques under the PBF category. Three-dimensional metallic parts are built by the continuous selective melting and fusing of metal powder layers based on the initial computer-aided design (CAD) data, often with distinctive microstructures and properties comparable to those of conventionally manufactured (CM) materials. Although previous studies on SLM largely focused on processing single metallic materials (metals and alloys) at one time, the increasing importance of multi-material components in many engineering applications, e.g., automotive and biomedical industries, has accelerated research on the SLM fabrication of multiple metallic materials, generally termed multi-material AM (MMAM), such as 316L SS with Cu alloys, e.g., CuSn10, C18400, and C52400 [4–7], and Inconel alloys, e.g., IN 625 and IN 718 [8–11]. In particular, 316L SS/IN 718 parts have been widely used for engineering applications that require high toughness strength, excellent corrosion and oxidation resistance, and good creep or fatigue resistance and operate in harsh working conditions such as in nuclear power plants, aerospace engine/repair parts, gas turbines, and oil and gas industries. Some specific uses of such dissimilar material combinations include advanced blading systems for industrial gas turbines [12], a hot-side heat exchanger for a fission surface power conversion system by The National Aeronautics and Space Administration (NASA) [13], tube (316L SS) and quick disconnect (IN 718) components of the external active thermal control systems for the International Space Station (ISS) [14], and pressure tubes for nuclear fission reactors [15], and these material combinations are used in many other applications involving operation in high-temperature conditions.

Until now, the investigations on the SLM fabrication of 316L SS/IN 718 have mainly focused on the multiple-powder dispensing mechanisms (machine aspect) [8,9] and the microstructural characterisation and mechanical testing of the interfacial region (materials science aspect) [16–18]. For example, Mei et al. [17] and Mohd Yusuf et al. [18] observed strong metallurgical bonding in the interfacial region having a width of ~100 µm. Wen et al. [16] and Mohd Yusuf et al. [18] reported higher hardness in the interfacial region compared to the 316L SS area, albeit lower than that in the IN 718 region. However, the detailed microstructure-influenced mechanisms of strengthening of the interfacial region are still not clear. Thus, this study attempts to address such deficiencies by conducting a detailed investigation of the interfacial microstructures, hardness, and strengthening mechanisms of MMAM 316L SS/IN 718 fabricated by SLM (henceforth referred to as MM SLM). The manufacturing process was achieved via a self-developed MM SLM system equipped with a novel multiple-powder deposition system. Detailed characterisations and testing were conducted using various microscopy techniques, energy dispersive X-ray spectroscopy (EDX), X-ray diffraction (XRD), and Vickers hardness (HV) and nanoindentation measurement techniques to determine the evolution of interfacial microstructures

and hardness through the interfacial as well as the individual 316L SS and IN 718 regions. A strengthening model was then established to assess the contribution of different strengthening components to the overall strength of the interfacial region of this MM alloy.

2. Materials and Methods

2.1. Material and Sample Preparation

Gas-atomised 316L SS and IN 718 powders were used in this study, and their respective elemental compositions based on EDX analysis are shown in Table 1. It is known that both alloys possess the same γ-austenite FCC crystal structure, similar lattice parameters and coefficient of thermal expansion (CTE) values, and high mutual solubility.

Table 1. Chemical composition of 316L SS and IN 718 powders used in this study as determined via EDX analysis (wt. %).

	Cr	Ni	Nb	Ti	Mo	Mn	Si	C	P	S	Fe
316L SS	18.43	12.2	-	-	2.46	1.86	0.03	0.013	0.032	0.01	*Bal.*
IN 718	18.6	50.7	5.01	0.89	3.1	0.04	0.09	0.016	0.013	-	*Bal.*

2.2. Multi-Material SLM System and Processing Parameters

An in-house-built MM SLM machine (HK PM250) self-developed at the University of Southampton was used to fabricate MM 316L SS/IN 718 samples. This machine is equipped with a continuous fibre laser unit (laser focus diameter: 100 µm) comprising a high-speed and high-precision galvanometer scanning system, an f-θ lens, and a multi-powder feeding system, as shown by the schematic diagram in Figure 1. With a build area of 250 × 250 × 280 mm (x-, y-, and z-, respectively), this machine utilises argon to provide an inert chamber environment and a set operating temperature of 21 °C.

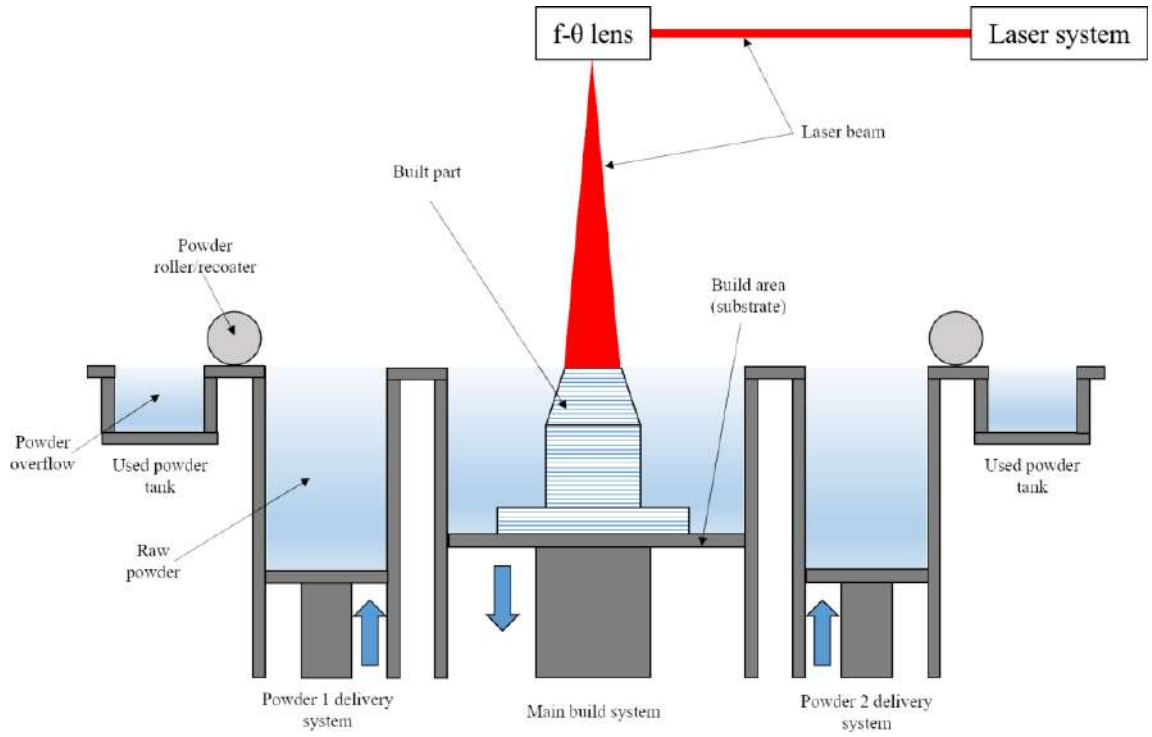

Figure 1. Schematic of HK PM 250 3D printer.

Before proceeding with the MM SLM fabrication, the processing parameters for both materials were optimised by conducting orthogonal experiments to achieve a high densification level (>98%) and low porosity content. The optimised processing parameters

used to fabricate the samples in this study are as follows: laser power (P_L), 300 W; scan speed (v), 900 mm s^{-1}; layer thickness (d_L), 30 µm; scan line spacing (h_L), 80 µm; and unidirectional scan strategy rotated 90° between each layer. The volumetric energy density (VED), a quantity that is often used to correlate various L-PBF processing parameters via the relationship $E = P_L/v^*h_L^*d_L$, is calculated as 138.8 J mm^{-3} in this study.

Figure 2a shows the schematic diagram of a 10 × 10 × 50 mm rectangular bar built on a 304L SS substrate on the x-y plane parallel to the z-direction using this machine via alternate deposition, melting, and solidification of successive 316L SS and IN 718 powder layers [18]. In total, the completed rectangular bar comprises 5 smaller blocks of 316L SS and 5 smaller blocks IN 718 materials alternately stacked on top of each other (10 × 10 × 5 mm each) as shown in Figure 2b.

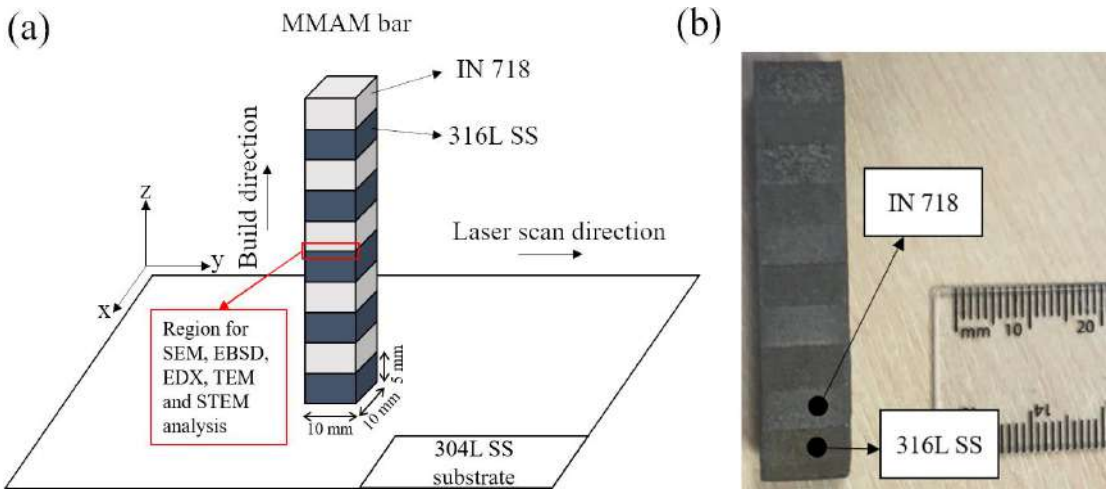

Figure 2. (**a**) Schematic of the MM build [18]; (**b**) the as-built MM rectangular bar. Figure 2a reproduced with permission from [18], Elsevier, 2020.

2.3. Microstructural Characterisation

Microstructural characterisation was conducted at the interface of the solidified joint, i.e., in the interfacial region between two different materials (316L SS and IN 718), as highlighted by the arrow and description in Figure 2a. Wire electrical discharge machining (EDM) was used to section the required test specimens, which were then mounted on bakelite and ground using SiC papers with gradually increasing grit numbers (120–4000). Subsequently, the ground specimens were polished to a mirror-like surface finish using 3 and 1 µm diamond suspensions before being etched with Kallling's No. 2 reagent. The melt pools and cellular sub-structure colonies, two common microstructural features of AM-fabricated metallic materials, were then revealed via optical microscopy (OM) and scanning electron microscopy (SEM) observations, conducted using an Olympus BX-51 optical microscope (Evident, Olympus Scientific Solutions, MA, USA) and a JSM-JEOL 6500 FEI SEM (JEOL, Tokyo, Japan), respectively.

The grain structures (size, morphology, and crystallographic orientation) were determined by using electron backscatter diffraction (EBSD) via a digital HKL Nordlys F++ camera (Oxford Instruments, High Wycombe, UK) that was coupled with the JSM-JEOL 6500 FE-SEM machine. EBSD specimens were prepared following the previously given grinding–polishing steps, but the etching stage was replaced by further mechanical polishing using colloidal silica having an average particle size of ~0.05 µm. These specimens were then subjected to electropolishing in an 80:20 methanol to perchloric acid ratio electrolyte mixture at 16 V and 0.5 A for 18 s. EBSD images were taken for 100 × 100 µm areas within the interfacial region with a step size of 0.1 µm that covers about 100 grains per area,

followed by quantitative and qualitative evaluations through Aztec HKL software version 2.0 (Oxford Instruments, High Wycombe, UK).

Deeper interfacial microstructures such as dislocation networks and secondary phases/precipitates were examined via transmission and scanning transmission electron microscopy techniques (TEM and STEM, respectively). In preparation for TEM/STEM, the small blocks were further cut to a thickness of ~80 µm using wire EDM, followed by the punching out of smaller disks (3 mm diameter) in the interfacial region. Finally, thin lamellae were extracted from these disks by using a Gatan dimple grinder (model 656) and a Gatan PIPS II precision ion polishing system (Gatan Inc., Pleasanton, CA, USA). TEM/STEM observations were then performed using an FEI Talos TMF200 TEM/STEM instrument (mThermo Fisher Scientific, Waltham, MA, USA) equipped with an energy dispersive X-ray spectroscopy (EDX) detector (FEI, Brno-Cernovice, Czech Republic).

X-ray diffraction (XRD) analysis was conducted using a Rigaku SmartLab X-ray Diffractometer (Rigaku, Tokyo, Japan) to quantitatively evaluate the phase composition and dislocation density in the interfacial region of the as-built MM alloy. The XRD instrument is equipped with a graphite monochromator using CuKα radiation. XRD measurements were carried out with 10 steps per degree and a count time of 1 s per step on the instrument. A slit length of 5 mm was chosen for measurements on the IN 718 and 316L SS regions, and a slit length of 2 mm was chosen for measurements on the interface of the small blocks. The phase composition and dislocation density information were determined from the resulting XRD peaks and line broadening data by using the Materials Analysis Using Diffraction (MAUD) software (MAUD, version 1.999, L. Lutterotti, Italy) based on the Rietveld refinement method [19–21].

2.4. Hardness and Nanoindentation Measurements

Microhardness measurements were taken across the 316L SS, interfacial, and IN 718 regions along the rectangular bar using Future Tech FM-300 Vickers hardness (HV) instrument (Future-Tech Corp, Kawasaki, Japan) with an applied load of 100 gf, and a dwell time of 15 s. Individual HV values were taken at 0.6 mm between each main indent, and four further indentations were made around each main indentation with a fixed distance of 0.3 mm to obtain the average value and error bar for each location. The HV value at each location was estimated by averaging a total of five indentations. These measurements provide detailed information on the evolution of HV values across the different material regions. On the other hand, a nanoindentation instrument (NanoTest Vantage System, Micromaterials Ltd., UK) with a three-sided pyramidal Berkovich indenter and a centreline-to-face angle of 65.3° was used to determine the hardness within the interfacial region. The nanoindentation measurements were taken under a constant peak load, P_{max}, of 50 mN at a constant strain rate, $\dot{\varepsilon}_i$, of 1.25×10^{-4} s^{-1}. The nanoindentation results were normalised by correcting the readings upon consideration of the presence of thermal drift, which was maintained below 0.1 nm s^{-1} throughout the testing period. The total coverage distance was 200 µm, with the distance between each indent set to 10–20 µm. The nanohardness, H, value at each location was averaged from five different indents (the main indent and four other indents around it).

3. Results

3.1. Interfacial Microstructures

The interfacial region comprises a narrow, ~100 µm wide fusion zone (FZ), as well as unmixed IN 718 and 316L SS areas within its proximity, each ~0.5 mm on either of its sides. Distinct Fe- and Ni-rich regions can be observed in the interfacial region, as illustrated in the EDX maps in Figure 3a,b by the dark pink and dark purple, respectively. Meanwhile, the lighter pink and lighter purple, respectively, demonstrate continuous and coherent fusion of Fe and Ni in the FZ that suggest significant Fe and Ni dilution and interfacial diffusion across 3–4 layers of powder bed depositions attained via the 30 µm layer thickness utilised in this study. Such characteristics are indicative of sound metallurgical bonding

that has been achieved through the MM SLM processing. Furthermore, the high cooling rates in PBF AM processes (10^5–10^8 Ks^{-1}) have avoided the formation of a HAZ, which is often associated with brittleness, low joint strength, and high corrosion susceptibility in conventional fusion welding [15].

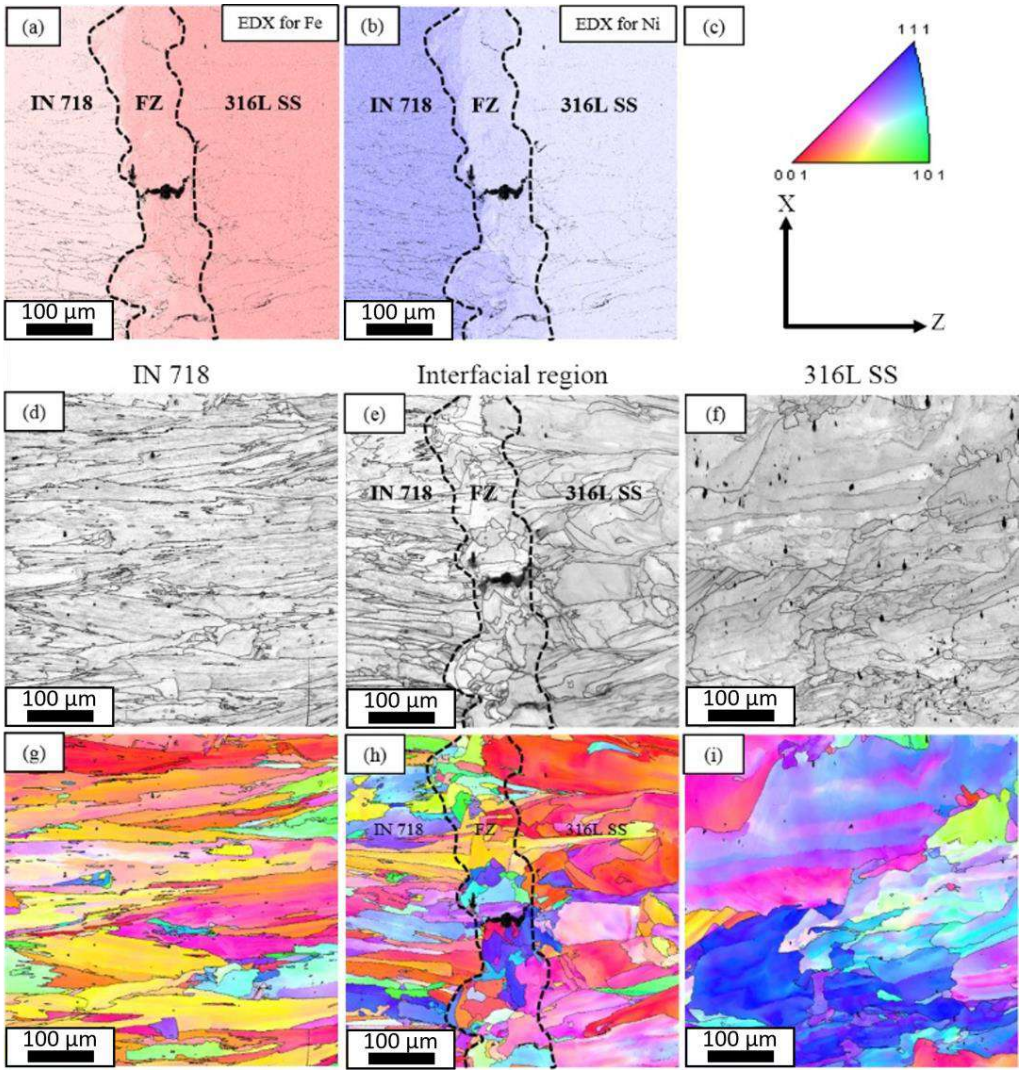

Figure 3. (**a**,**b**) EDX maps of the interfacial region [18], (**c**) inverse pole figure (IPF) colour legend (x-z plane indicates build direction), (**d**–**f**) BSE images exhibiting porosity in different areas of the MM SLM specimen, and (**g**–**i**) EBSD maps exhibiting crystallographic orientation in the respective areas of the MM SLM specimen. Figure 3a,b reproduced with permission from [18], Elsevier, 2020.

Small irregular-shaped, process-induced pores are shown across the interfacial region, as well as the individual IN 718 and 316L SS regions, through the as-built specimens, with a relatively larger elongated pore visible centrally across the FZ in the backscattered electron SEM (BSE-SEM) images in Figure 3d–f. However, no cracks are detected throughout the as-built structure. The presence of such pores, also known as lack-of-fusion porosity, is common in additively manufactured metallic materials due to inadequate molten pool penetration into previously and successively deposited powder bed layers, resulting from insufficient energy density parameters, e.g., laser power, scan speed, scan line spacing, and layer thickness [22]. In particular, the larger elongated pore in the FZ can be associated with the difficulty of obtaining a single set of optimised processing parameters due to the slightly contrasting intrinsic properties of both alloys, e.g., thermal conductivity and CTE [23]. Nevertheless, the overall porosity content in the MM SLM specimen is determined

to be only ~0.81%, suggesting a high level of densification (>99%) is still achieved upon solidification [18].

The colour-coded inverse pole figures (IPFs) in Figure 3g–i clearly show a mixture of grain size distribution without any preferred crystallographic orientation in the interfacial region as well as the individual IN 718 and 316L SS regions. Fine and coarse elongated columnar grains with average grain sizes of 55 ± 5 µm and 85 ± 3 µm are attained in the unmixed 316L SS and IN 718 areas within the interfacial region and in the corresponding individual material regions, respectively, suggesting a directional grain growth despite the lack of preferential crystallographic orientation. Interestingly, the FZ reveals fine, equiaxed grains with an average size of 45 ± 3 µm, which can most likely be associated with the abrupt change of material, i.e., from 316L SS to IN 718 and vice versa, as well as several thermal excursions that occur inside of the fused 3–4 powder layers.

Meanwhile, Figure 4a clearly distinguishes the unmixed IN 718 and 316L SS centrally in the FZ as shown by the distinct contrast in the etching of both materials. This is further illustrated by a sharp FZ boundary that divides the unmixed material regions denoted by the red dashed line in Figure 4b. Closer inspection of the cellular sub-structures in the sharp FZ reveals fine columnar dendritic cells as well as a combination of fine equiaxed and columnar cells in the unmixed IN 718 and 316L SS (all sub-micron sized). Regardless of their morphologies, the cells are able to fuse together cohesively across the boundary of both materials (dashed red line, Figure 4b), which further signifies good metallurgical bonding in the FZ and in the overall interfacial region. On the other hand, Figure 4c exhibits single-grain structures growing through several melt pools in the individual IN 718 region, while Figure 4e shows multiple-grain structures growing within a single melt pool in the individual 316L SS region. Nevertheless, the zoomed-in areas A (Figure 4c) and B (Figure 4e) shown by the high-magnification SEM images in Figure 4d,f, respectively, both demonstrate the growth of cellular sub-structures with a particular direction within a melt pool ending at the melt pool boundary (MPB) before growing at different orientations in a new melt pool.

In addition, Table 2 lists the chemical composition along the FZ (Figure 4a) based on EDX area scan analysis. The results suggest a homogeneous distribution of Fe (from 316L SS) and Ni matrix (from IN 718), with higher Nb and Ti wt.% compared to their initial contents in the IN 718 powder (~5.1 and ~0.89 wt. %, respectively).

Table 2. EDX analysis of the chemical composition along the FZ (wt. %).

Cr	Ni	Nb	Mo	Ti	Mn	Fe
20.34	32.7	9.55	3.6	1.21	0.02	*Bal.*

Figure 5 depicts TEM and STEM images taken in the interfacial region, revealing sub-micron and nanoscale microstructural features that include dislocation tangling networks and secondary-phase precipitates. In particular, the equiaxed (bright-field (BF) TEM, Figure 5a) and columnar (BF TEM, Figure 5b) cellular sub-structures can be considered as dislocation cells that form as a result of high internal stresses experienced during the MM SLM process [24]. In addition, the thick boundaries surrounding these cells are often ascribed to the accumulation of dislocations and/or segregation of heavier elements here [24]. Furthermore, the dislocation networks observed in the BF TEM shown in Figure 5c have much higher density compared to those typically seen in annealed CM alloys [25]. Moreover, denser dislocation tangles and pileups observed at the boundaries of two adjacent equiaxed cells compared to their interior (BF TEM, Figure 5d) suggest a preferential location for the concentration of dislocations.

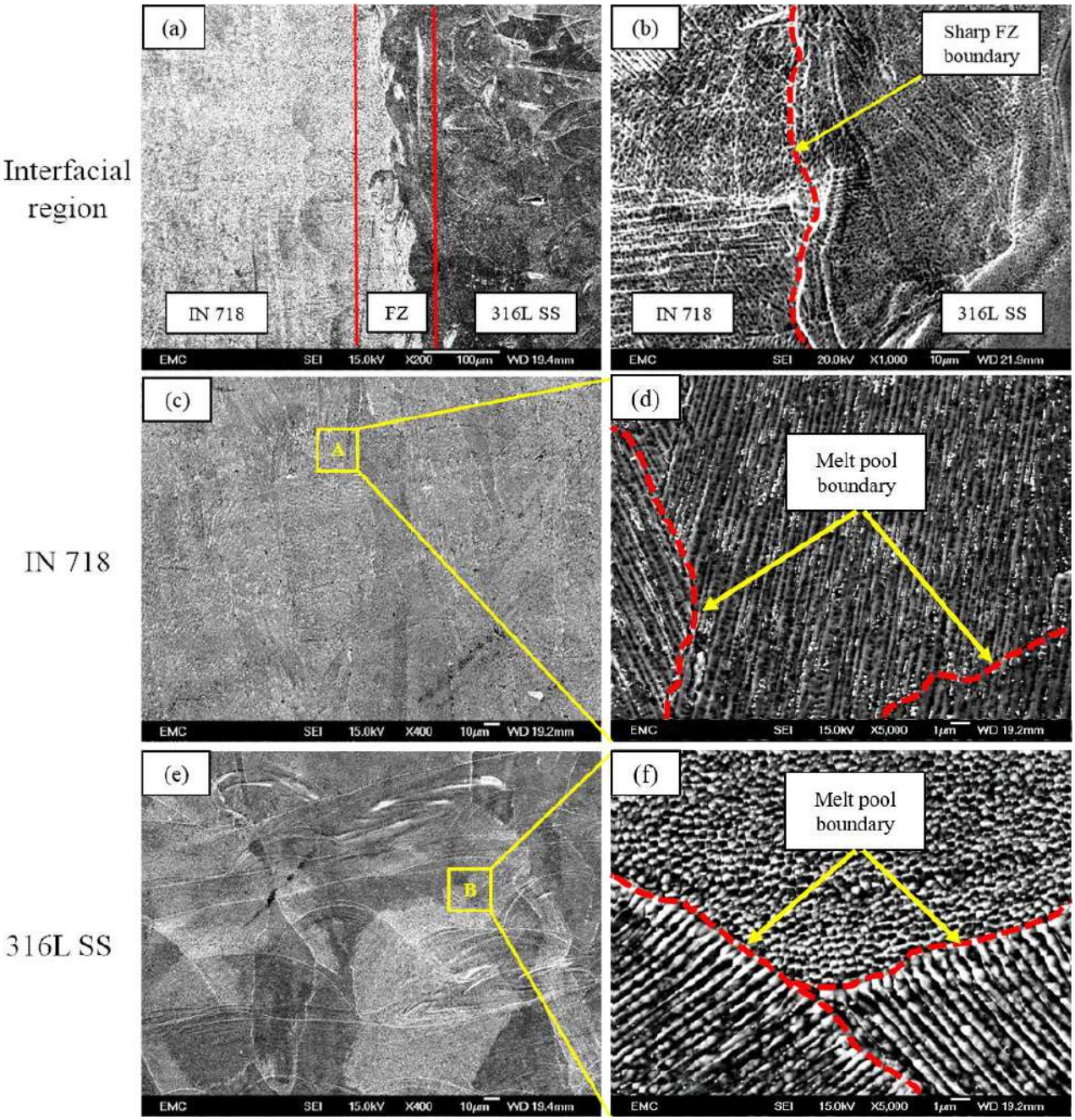

Figure 4. SEM images taken parallel to the build direction of the test specimen showing the (**a**) overall and (**b**) sharp FZ boundary of the interfacial region, growth of (**c**) grains and (**d**) cellular sub-structures through the MPBs in the individual IN 718 region, and growth of (**e**) grains and (**f**) cellular sub-structures through the MPBs in the individual 316L SS region.

On the other hand, the formation of Laves phase, characterised by the chemical formula $(Ni,Fe)_2(Nb,Ti,Mo)$, with irregular-shaped morphologies is evident in the BF TEM shown in Figure 5e, whereas examples of spherical carbide precipitate, (Nb,Ti)C, formed after MM SLM processing can be seen in the BF TEM shown in Figure 5f. Table 3 shows the average elemental compositions (in wt.%) for the Laves phase and carbides based on EDX analysis of these particles. Further, through ImageJ software analysis of the TEM and STEM images, their average fraction and diameter are determined as ~1.87 vol.% and ~30.58 nm, respectively. Figure 5g displays a high-angle annular dark field STEM (HAADF-STEM) image of equiaxed cell boundaries with corresponding EDX area maps

(Figure 5h–m); a similar HAADF-STEM image showing the boundaries of a columnar cell and corresponding EDX area maps are also shown in Figure 5n,o–t, respectively. Homogeneous dispersions of Fe, Ni, and Cr within the matrix and the segregation of the heavier Nb into the cell boundaries are clearly observed for both cases. The EDX area maps also confirm that the black spherical particles in Figure 5g,n are all Nb- and Ti-rich carbides indeed.

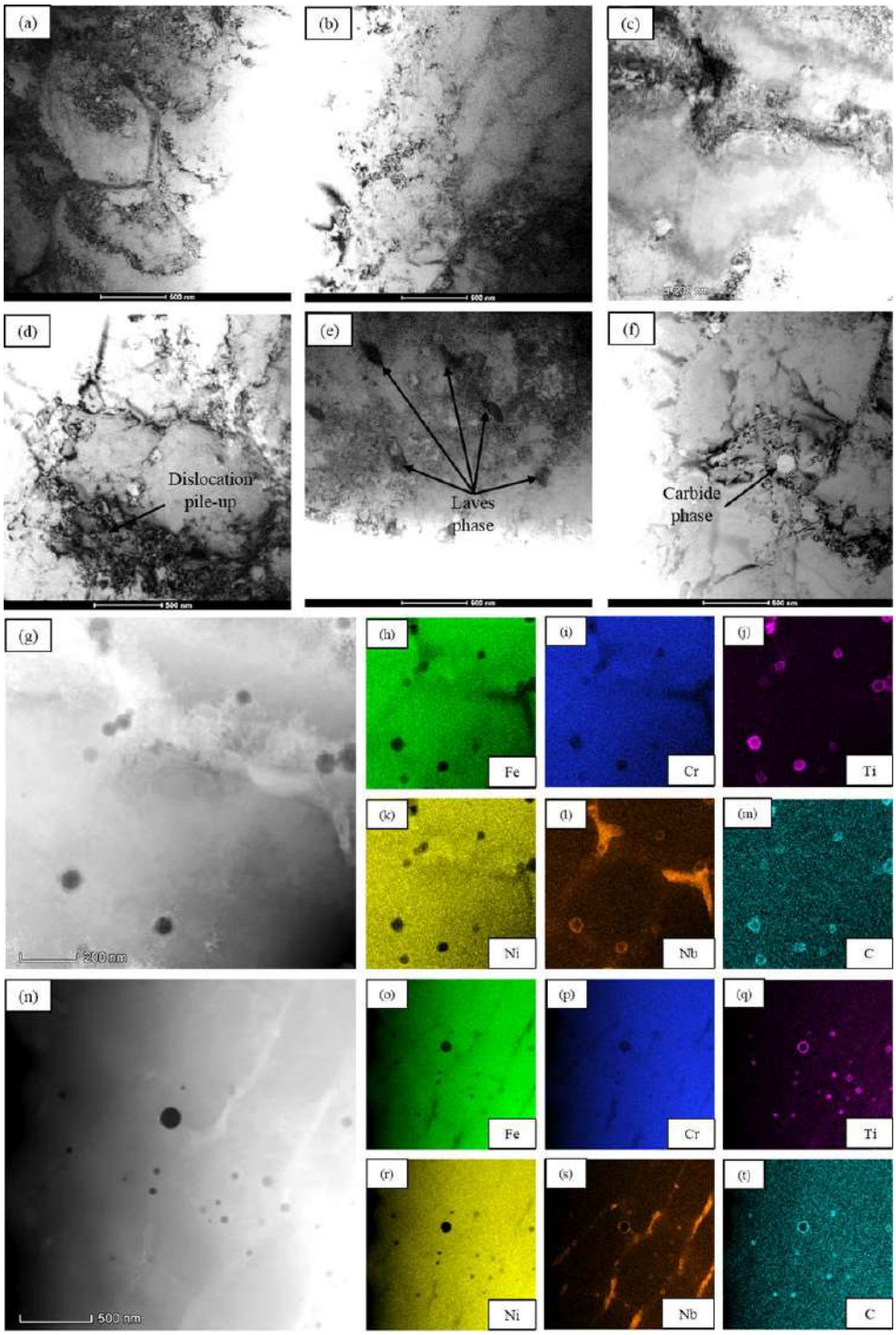

Figure 5. (**a**–**f**) BF TEM images; (**g**,**n**) HAADF-STEM images; (**h**–**m**) EDX maps for (**g**) and (**o**–**t**) EDX maps for (**n**) for specific areas in the interfacial region.

Table 3. Average chemical composition for Laves phase and carbide particles shown in Figure 5 obtained from EDX analysis (wt. %).

Precipitates	Cr	Ni	Fe	Nb	Mo	Ti
Laves	17.54	45.23	12.22	19.13	4.72	1.16
Carbide	10.56	6.55	3.38	39.82	1.64	38.05

3.2. XRD Analysis

The XRD spectra obtained from XRD measurements in the interfacial and individual IN 718 and 316L SS regions are shown in Figure 6.

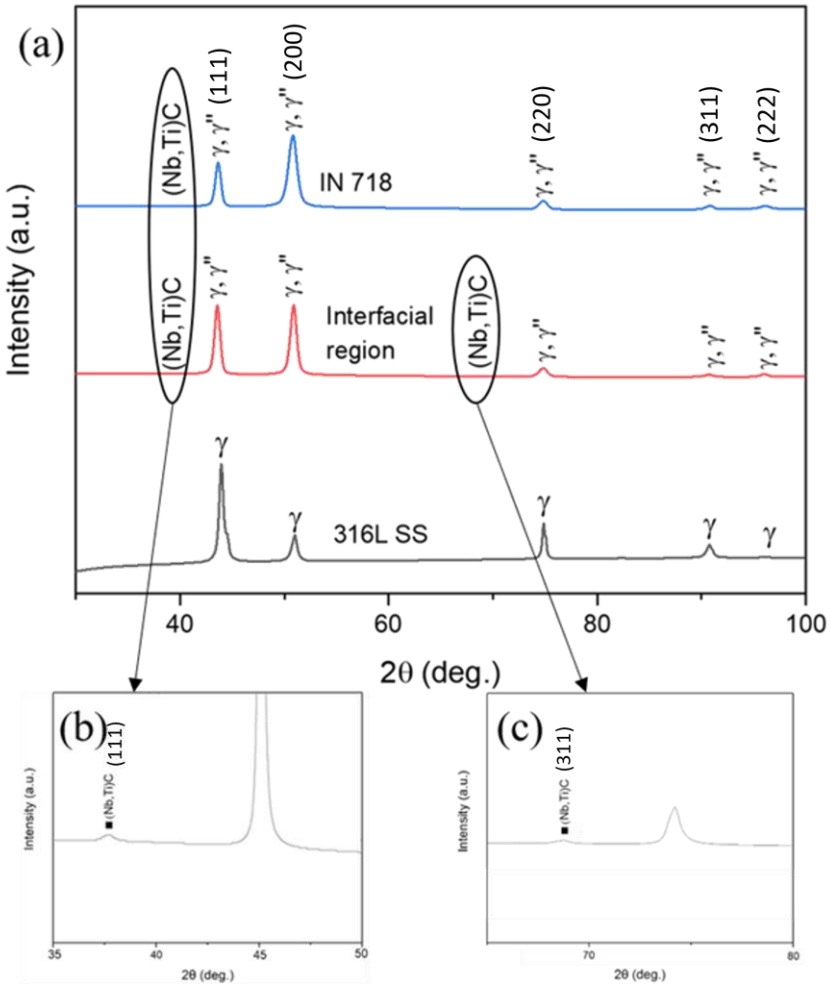

Figure 6. (**a**) XRD spectra for the interfacial and individual material regions, (**b**,**c**) zoomed-in diffraction patterns of the weak (Nb,Ti)C signals from the main XRD spectra of the individual IN 718 and interfacial regions.

The XRD peaks primarily demonstrate the coinciding phases of γ-austenite face-centred cubic (FCC) and γ"-body-centred tetragonal (BCT) crystal structures; γ-FCC is the matrix phase for 316L SS and IN 718, while γ"-BCT is the main phase for the strengthening of IN 718. The γ"-BCT peaks are known to overlap with their γ-FCC counterparts in a typical IN 718 XRD spectra, thereby requiring TEM observations to identify and distinguish their structures and morphologies unambiguously [26]. Commonly, γ"-BCT structures are characterised as coherent disks with diameters of ~60 nm and thicknesses ranging from 5 to 9 nm, but such precipitates are not detected based on the TEM observations in this study, e.g., Figure 5. Thus, it can be reasonably inferred that the major XRD peaks

for the individual IN 718 and interfacial regions only correspond to the γ-FCC phase. In addition, weak peaks of (Nb,Ti)C can be observed in the individual IN 718 and interfacial regions (Figure 6b,c) that correspond well with the observation of Nb- and Ti-rich carbide precipitates based on the EDX area maps in Figure 5. On the other hand, the XRD results show that the 316L SS region exhibits peaks corresponding to a single γ-FCC structure only. Therefore, the XRD spectra results suggest that the overall MM SLM 316L SS/IN 718 in this study solidifies as a single γ-FCC structure without any phase transformation.

Subsequently, the average values of lattice microstrain $\langle \varepsilon^2 \rangle^{1/2}$ and crystallite size D_c in the interfacial region determined using the MAUD software through XRD line broadening analysis based on the Rietveld refinement approach are evaluated as ~0.198 and 280 $\pm$ 25 nm, respectively. Using this information, the value of dislocation density, ρ, in the interfacial region is then estimated based on the following equation:

$$\rho = \frac{2\sqrt{3}\langle \varepsilon^2 \rangle^{1/2}}{D_c \boldsymbol{b}} \quad (1)$$

where $\boldsymbol{b}$ is the Burgers vector, taken as 0.26 nm for both 316L SS and IN 718 [27,28]. Based on this formula, ρ in the interfacial region is quantified as 0.942 $\pm$ 0.5 $\times$ 10^{13} m^{-2}.

3.3. Hardness

The Vickers microhardness (HV) distribution across the interfacial and individual material regions shown in Figure 7 shows roughly consistent HV values in the individual IN 718 region up to ~2 mm towards the interfacial region, averaging at 306 $\pm$ 6 HV. The HV values then gradually decrease until a distance of ~2 mm from the FZ centre, before plateauing at an average value of 220 $\pm$ 10 HV in the individual 316L SS region. Meanwhile, the average HV value in the interfacial region is measured as 260 $\pm$ 9 HV. These results are fairly consistent with the HV values measured in similar literature investigating MMAM of 316L SS/IN 718 combinations [9,15,18]. Although the γ''-BCT precipitates are known as the main strengthening mechanism (precipitation strengthening) of IN 718, their absence in this study would suggest other mechanisms that contribute to the higher hardness of the individual IN 718 and interfacial regions compared to the lower hardness in the individual 316L SS region.

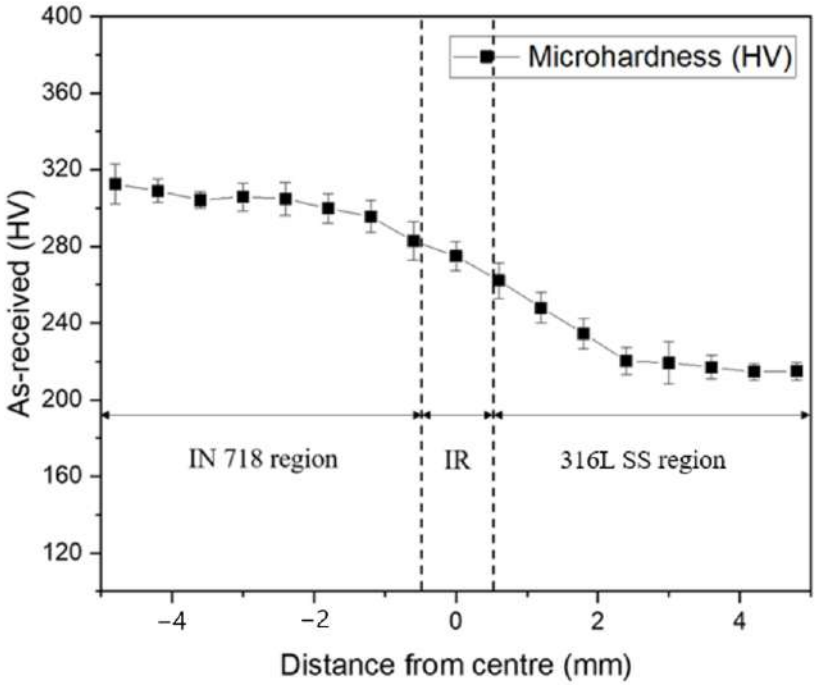

Figure 7. HV distribution across the interfacial and individual material regions.

This is because the cellular sub-structures formed due to the high-stress conditions during AM processing are found to become sites for dislocation accumulation, yielding dense dislocation networks that inhibit dislocation motions, thereby strengthening AM-fabricated metallic materials through dislocation strengthening [23,24]. In fact, the value of ρ in the interfacial region has been determined as $0.942 \pm 0.5 \times 10^{13}$ m^{-2}, which is higher than $0.69 \pm 0.5 \times 10^{13}$ m^{-2} evaluated in the individual 316L SS region [29]. In addition, carbide precipitates have also been found as effective sites for the impediment of dislocation motions to enhance the strength of metallic materials via precipitation hardening [30,31]. Hence, the (Nb,Ti)C precipitates found in the interfacial region in this study are inferred to provide precipitation hardening in the absence of γ''-BCT precipitates. Other than that, it is known that the hardening (or strengthening) of any CM- or AM-fabricated metallic materials is contributed by solid solution strengthening via the alloying elements of the particular material, as well as grain boundary strengthening. Thus, the additional contribution of dislocation hardening through the denser dislocation networks, precipitation hardening through the (Nb,Ti)C precipitates, and solid solution hardening provided by the alloying elements of both 316L SS and IN 718 could explain the higher average HV value of the interfacial region, in contrast with the lower hardness of the individual 316L SS region.

Although the HV measurements provide some information on the evolution of hardness through the interfacial and individual material regions, the hardness variation within the interfacial region and particularly inside the FZ is still unclear. This is due to 0.1 mm distance limit of the HV indenter, which means that the hardness within the narrow FZ (~100 μm) could not be precisely captured, thereby necessitating the use of nanoindentation measurements through the interfacial region. A total distance of 200 μm is covered by the nanoindentation instrument, 100 μm within the FZ and another 50 μm each on either side of the FZ boundary into the unmixed IN 718 and 316L SS areas. Each indent is spaced at 10 μm and 20 μm inside the FZ and in the unmixed areas, respectively. For each location, the average nanohardness, H, value is taken from five indents, one main indent at a selected area and another four indents surrounding it, with the results shown in Figure 8a.

Inside the interfacial region, the nanohardness, H, distribution (Figure 8a) actually exhibits a similar trend to the HV measurements taken across the interfacial and individual material regions (Figure 7). Consistently higher H values are attained in the unmixed IN 718 area (~5–6 GPa) compared to the unmixed 316L SS side (~3–3.5 GPa), with the FZ having H values between those in both unmixed material sides (~4–5 GPa). Meanwhile, the mean distribution of the matrix elements (Fe and Ni) and other alloying elements (Cr, Nb, Ti, and Mo) in the interfacial region obtained through EDX line scan analysis is shown in Figure 8b. The Fe and Ni concentrations vary roughly linearly across the FZ and the unmixed sides, without much variation in the concentrations of Cr and Mo. Interestingly, small levels of Nb and Ti are detected in the unmixed 316L SS side even though they are absent in the initial 316L SS feedstock powder. The unlikely presence of both elements there can possibly be caused by (i) incomplete powder removal/cleaning prior to the changing of feedstock powders from IN 718 to 316L SS that results in powder contamination, (ii) the preferred segregation of the heavier Nb into the cellular sub-structure boundaries that may result in the formation of NbC in the unmixed 316L SS side due to the affinity between Nb and C upon deposition of a new IN 718 powder layer onto a 316L SS layer that has solidified previously, or (iii) both.

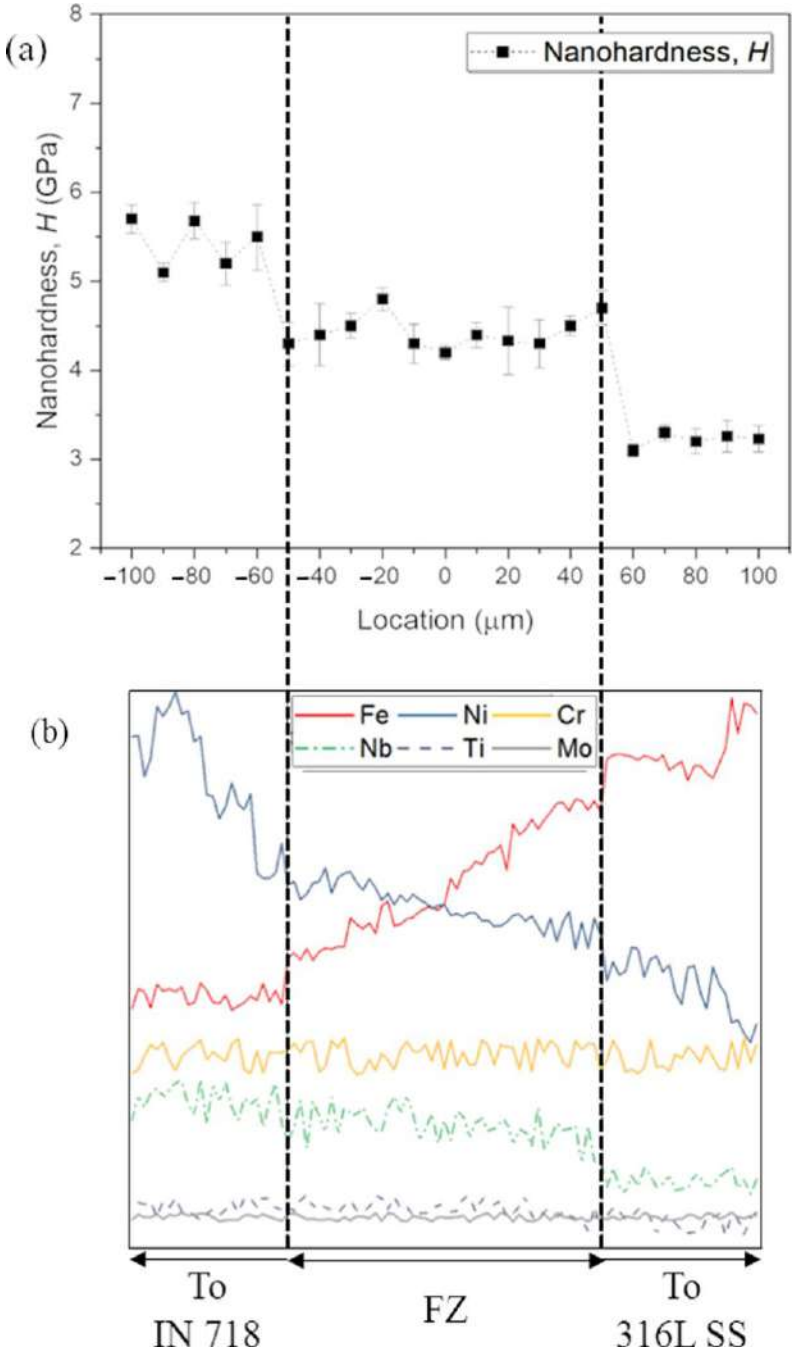

Figure 8. (**a**) Distribution of *H* values and (**b**) concentrations of matrix (Fe and Ni) and other major alloying elements (Cr, Nb, Ti, and Mo). Both results are based on respective nanoindentation measurements and EDX line scans taken inside the interfacial region.

4. Discussion

4.1. Interfacial Microstructures

In this study, an in-house-developed MM SLM system was used to additively manufacture MM 316L SS/IN 718 samples with high densification levels (>99%) successfully. The microscopy images in Figure 3 exhibit an interfacial region comprising a narrow, ~100 μm wide intermixed Fe and Ni fusion zone (FZ) and unmixed 316L SS and IN 718 areas. The interfacial diffusion of Fe and Ni clearly determines the thickness of the FZ, in which its distance is found to be governed by the layer thickness and scan speed processing parameters [4,5,32]. For example, a layer thickness of 30 μm with varied scan speeds

between 700 and 1200 mm s^{-1} was used by Chen et al. [4] to attain ~550 µm wide FZ in their SLM-fabricated 316L SS/CuSn10 specimens. Meanwhile, Sing et al. [32] obtained an FZ width of ~200 µm for their MM SLM AlSi10Mg/C18400 specimens when the layer thickness was set as 50 µm and the scan speeds ranged from 400 to 1140 mm s^{-1}. In addition, Liu et al. [5] determined the width of the FZ as ~750 µm for SLM-manufactured 316L SS/C18400 samples when using a layer thickness of 50 µm and changing the scan speeds in the range of 150–400 mm s^{-1}.

Regardless, the findings in this study demonstrate significant and cohesive dilution and diffusion among the individual matrix elements (Fe and Ni), suggesting a good metallurgical bonding throughout the interfacial region. These can be ascribed to the constant partial re-melting of previously solidified layers and melting of successive powder layer depositions that create sound metallurgical bonding typically attained in cladded metal/alloy components [5]. The partially re-melted topmost part of a previously solidified 316L SS layer mixes with a freshly deposited and melted IN 718 powder layer to result in a high Fe percentage in the new solidified IN 718 layer. Meanwhile, subsequent deposition, melting, and fusion of successive IN 718 powder layers gradually decrease and increase the percentages of Fe and Ni, respectively. This steadily occurring phenomenon ends at the FZ boundary where the Fe percentage reaches a minimum, and Ni nears its original wt.% in the IN 718 powder, beyond which only IN 718 powders are being melted and fused together (Figure 8b). Such observations suggest a gradual variation of the Fe and Ni matrices inside the FZ as compared to an abrupt elemental change that may enhance the bonding strength in the interfacial region [4].

On the other hand, a directional growth trend of columnar grains and cellular sub-structures approximately parallel to the build direction (x-z plane) is evident in the unmixed areas within the interfacial region and in the individual material regions (Figures 3 and 4). These are usual phenomena in PBF AM-fabricated metallic materials that happen when the partially re-melted solidified layers turn into effective sites for grain nucleation and growth in subsequent powder layer depositions [31,33]. Furthermore, the directional growth of grains and cells through different melt pools across several layers of powder bed observed in Figure 4c–f has been found to be influenced by a number of factors, including scan strategy (processing parameter), as well as temperature gradients, cooling rates, and heat transfer modes (physical phenomena) in the SLM process [25].

Furthermore, studies have shown that the superior heat conduction through solidified layers compared to heat conduction through unsolidified powder particles and heat convection between the melt pools and the surroundings results in considerably high cooling rates (10^5–10^8 Ks^{-1}) in PBF AM processes [25,34]. Accordingly, rapid directional solidification that facilitates columnar grain growth parallel to the build direction is favoured, which most likely explains the formation of columnar grains on the x-z plane shown in Figure 3. However, other researchers explained that the direction of temperature gradient and heat flux (thermal conditions) can actually be rotated to different orientations by manipulating the scan strategy and therefore does not necessarily need to be exactly parallel to the build direction [35,36]. Hence, the alternate 90° rotation of the unidirectional scan strategy employed for each layer during the MM SLM processing in this study could possibly explain the lack of preferential crystallographic orientation observed in Figure 3.

Apart from influencing the directional grain growth, the thermal conditions also govern the nucleation and growth of the cellular sub-structures [35]. Continuous growth of columnar cells with similar directions across several melt pools can only occur only if the localised thermal conditions at certain laser-scanned locations on the powder bed prefer such directional growth. Otherwise, their growth direction will follow that of the more thermally favoured one in the new melt pool. The columnar cells in this study can be observed to nucleate in a stop–start manner as shown in Figure 4. This means that the growth of such cells in a specific direction within a single melt pool produced by laser-scanning a particular area ends at the MPB, before growing in different directions in other melt pools upon laser beam irradiation at other powder bed locations. Thus, it is

reasonable to attribute this unique cellular sub-structure growth pattern to the constantly changing movements of the laser beam based on the set scan strategy, which continuously alters the direction of heat flux and generates various localised temperature gradients.

Meanwhile, the relatively coarser 316L SS columnar grains averaging at 85 ± 3 μm compared to the IN 718 counterparts that average at 55 ± 5 μm shown in Figure 3d–i could be attributed to the marginally higher CTE of 316L SS (~16 μm m^{-1} $°C^{-1}$) compared with that of IN 718 (~13 μm m^{-1} $°C^{-1}$), thereby enabling larger expansions of area and volume of the grain structures within a particular temperature gradient. However, the fine equiaxed grains averaging at 45 ± 3 μm observed in the FZ (Figure 3e–g) are rather unusual. Nevertheless, they could possibly be caused by (i) the discrete change of materials from 316L SS to IN 718 and vice versa and (ii) steadily changing thermal conditions occurring through the 3–4 layers of fused powder particles there due to the rapid heating/cooling cycles of PBF AM processes. The combination of these two factors may produce steeper thermal gradients that are able to restrict grain nucleation and growth, yielding fine equiaxed grains composed of Fe and Ni matrices in the FZ [5].

Other than grains and cellular sub-structures, the mechanical properties of AM-fabricated metallic materials are also influenced by phase distribution and the presence of secondary phases/precipitates [22,34]. In the present study, XRD analysis in the interfacial region (Figure 6a) reveals peaks that strongly correspond to the overlapping of γ-FCC (austenite matrix of both 316L SS and IN 718) and γ''-BCT (main strengthening phase for IN 718) phases. The latter crystal structure is typically associated with the Ni_3Nb precipitates formed in solidified IN 718 structures due to the presence of Nb as one of its alloying elements. However, the coherent nature of both the BCT structure and the γ matrix results in peak signals that are usually associated with γ-FCC austenitic structures [36]. Additionally, weak signals related to XRD peaks for (Nb,Ti)C (carbide phase) are also detected in the interfacial region (Figure 6), corroborated by their presence as spherical entities along the boundaries of the cellular sub-structures (mostly NbC) and within the matrix of the region (largely TiC) as shown in Figure 5g–t. No identifiable signals of Laves phase are obtained from the XRD spectra, most likely due to its considerably low vol. % despite its presence in the form of fine and discrete, irregularly shaped particles there (Figure 5e). However, the absence of any noticeable γ''-BCT (Ni_3Nb) precipitates in this study even via TEM observations suggests that the precipitation hardening in the interfacial region could be contributed by the carbide phase precipitates instead.

The brittle nature of Laves phase, a common intermetallic compound in IN 718 structures formed due to the segregation of the heavy Nb element, makes it undesirable as it deteriorates the strength of this material [31]. The characteristic of very high heating/cooling rates that result in rapid solidification of melt pools proves to be a double-edged sword for PBF AM processes. This is because although it is capable of hindering heavy macrosegregations in IN 718 by inhibiting/impeding Laves phase growth [37,38], the occurrence of microsegregations is still largely unavoidable due to the fast solidification and growth of columnar grains and cells [39]. Thus, the effect of microsegregation is inferred to be the cause of Nb enrichment along the cellular boundaries seen in Figure 5g–t. Moreover, the known affinity of Nb and Ti towards C to form the respective carbides is associated with the observable presence of NbC along the cellular boundaries and TiC within the matrix, both in the interfacial region (Figure 5g–t). In fact, NbC and Laves phase can be formed along the boundaries of the cellular sub-structures via eutectic reactions: L $\rightarrow$ γ + NbC and/or L $\rightarrow$ γ + Laves [40]. Nonetheless, the weak peak signals of (Nb,Ti)C and the absence of peaks related to Laves phase in the XRD spectra (Figure 6) might be explained by the substantially low Laves phase and carbide contents in the interfacial region (~1.87 vol. %).

Contrastingly, no Mo segregation into cellular sub-structure boundaries or development of spherical Cr nanosilicates (inclusions) typically present in PBF AM-processed 316L SS can be detected in the interfacial region in this study. The former observation can be attributed to the relatively low content of Mo (~2.5 wt. %) in comparison with Nb (~5.01 wt. %) in the initial 316L SS and IN 718 feedstock powders, respectively, and

the higher microsegregation tendency of Nb compared to Mo resulting from its lower partition coefficient [38]. As for the latter finding, the formation of those nanosilicates has been associated with the high Si and Cr affinities towards O at elevated temperatures [24]. However, such nanoinclusions are very unlikely to manifest in the interfacial region in this study, possibly due to the nominal content of Si in the precursor 316L SS feedstock powder (~0.09 wt.%) and the inert Ar environment inside the build chamber that causes oxygen scarcity. Hence, it can be inferred that the microstructural features in the interfacial region are dominated by those typically attained in PBF AM-fabricated IN 718 rather than in its 316L SS counterpart, including precipitations of Laves phase ($(Ni,Fe)_2(Nb,Ti)$) and carbides (NbC and TiC), and cell boundary segregation of Nb. These are most probably the result of preferential Nb microsegregation inside the matrix and into the cellular sub-structure boundaries due to the relatively higher vol. % of this element than that of Mo in both precursor powders.

In addition, the dense networks of dislocation tangles observed at both matrix and cellular boundaries within the interfacial region (Figure 5a–d) are also prevalent in other PBF AM-fabricated metals and alloys. Quantitatively, the dislocation density, ρ, in the interfacial region determined by the MAUD software based on the XRD line broadening analysis is estimated as ~0.94×10^{13} m^{-2}, which is considerably greater than the 10^9–10^{10} m^{-2} range normally achieved in CM metallic materials [23,25]. The generation of dislocations in metallic materials is known to be the result of high internal stresses experienced during the manufacturing process. In the case of PBF AM processes such as MM SLM in this study, the characteristic high cooling rates and continuous rapid heating/cooling cycles result in repeated energy addition and removal to and from the processed material, inducing plastic deformation that causes internal stress pileups [24,37].

4.2. Hardening Mechanisms

It is known that the hardness/strength of a metallic material is ascribed to microstructural features such as the alloying elements, precipitates, dislocations, and grain boundaries. Thus, based on the microscopy observations in the interfacial region shown in Figures 3–5, the interfacial hardness for this MM SLM-fabricated 316L SS/IN 718 is contributed by the following mechanisms: (i) solid solution hardening through the friction stress of the crystal lattice structure and alloying elements of both materials; (ii) precipitation hardening via the (Ni,Ti)C carbides, since the primary Ni_3Nb precipitates are absent, while the insignificant Laves phase content does not have any effect on strength [37,38]; (iii) dense dislocation networks that impede dislocation motions to provide dislocation hardening; and (iv) grain boundary hardening through the fine equiaxed grains attained in this region. The average HV value in the interfacial region in this study is measured as 260 ± 9 HV, which is greater than those attained in fusion-welded 316L SS/IN 718 joints (~144–250 HV) [41–43] but is consistent with those achieved by SLM (~260–280 HV) [9,15]. The reason for superior interfacial hardness in AM-produced components can be ascribed to the greater dislocation densities and smaller grain sizes due to the characteristic rapid solidification that inhibits grain growth in comparison with fusion-welded joints of similar materials.

Altogether, the microstructural features mentioned previously account for respective hardening mechanisms that represent various obstructions towards dislocation motions, contributing to the overall hardness (HV) of the interfacial region. Therefore, the aim of this section is to provide quantitative assessments of the contribution of each hardening mechanism to the overall interfacial hardness based on the linear additive theory [44]. Here, the hardness–strength relationship is simplified for clarity via the empirical approximation $HV = kC\sigma_y$, where σ_y is the yield strength, k is the conversion multiplier between HV and σ_y and is taken as 9.8707, and C is a material-dependent constant valued as 3 for most FCC materials [45]. Hence, the overall hardness of the interfacial region, HV, can be analysed quantitatively as follows:

$$HV = HV_0 + \Delta HV_{SS} + \Delta HV_{ORO} + \Delta HV_\rho + \Delta HV_{GB} \quad (2)$$

where HV_0 is the intrinsic hardness of the material based on its friction stress, σ_0; ΔHV_{SS} is the contribution of solid solution hardening; ΔHV_{ORO} is the contribution of precipitation hardening; ΔHV_ρ is the contribution of dislocation hardening; and ΔHV_{GB} is the contribution of grain boundary hardening.

The values of friction stress, σ_0, for γ-Fe and γ-Ni crystal lattice structures are ~15.4 MPa and ~22 MPa, respectively [29,46,47]. It is reasonable to assume an equal contribution of both lattice structures here due to the comparable Fe and Ni wt. % values in the interfacial region based on the EDX area scan analysis in this study. Therefore, the average of these two values, calculated as 18.7 MPa or ≈6 HV, is taken as the numerical contribution of HV_0 here.

Meanwhile, the following equation can be used to evaluate the contribution of solid solution hardening:

$$\Delta HV_{ss} = C\sum k_i c_i^n \tag{3}$$

where k_i is the strengthening coefficient resulting from the dissolving of 1 wt. % of alloying element i inside the matrix, c_i is the concentration of alloying element i (wt.%), and n is a constant taken as 2/3 following the assessment of Goodfellow for Ni superalloys [48]. In this study, EDX area scans were conducted to determine the values of c_i for various alloying elements present within the interfacial region, whereas those of k_i are obtained from [48].

Within the interfacial region, the NbC and TiC particles present along the cellular sub-structure boundaries and inside the matrix become features that obstruct dislocation motions, resulting in their bypassing of the dislocations through Orowan looping, cross-slip, or particle-shearing mechanisms [49]. Secondary-phase particles/precipitates are known to enhance the strength of metallic materials through precipitation hardening regardless of the bypassing mechanism [50,51]. In this study, TEM observations in the interfacial region, presented in Figure 5c,d,f, show that the carbide particles tend to be bypassed via Orowan looping rather than being sheared through by the dislocations. Hence, the following equation can be used to evaluate the contribution from precipitation hardening through the Orowan looping mode:

$$\Delta HV_{ORO} = CM\Delta\tau_{ORO} = CM\frac{Gb}{\lambda_{ppt.}} \tag{4}$$

where M is the Taylor orientation factor (M = 3.05 for FCC materials) [52], b is the Burgers vector of the material (b = 0.26 nm for both alloys [27,28,46]), and G is the shear modulus of the material (G = 77,000 MPa for both alloys [52,53]). Meanwhile, $\lambda_{\mathrm{ppt.}}$ is the mean carbide spacing, estimated as follows:

$$\lambda_{ppt.} = \frac{4\left(1 - f_{ppt.}\right)r_{ppt.}}{f_{ppt.}} \tag{5}$$

where $f_{ppt.}$ is the mean vol. %, while $r_{ppt.}$ is the mean distance between each carbide particle.

The contribution of dislocation hardening, ΔHV_ρ, in the interfacial region can be estimated as follows:

$$\Delta HV_\rho = CM\alpha_1 Gb\sqrt{\rho_{Total}} \tag{6}$$

where α_1 is an empirical constant (α_1 = 0.3 [54]) and ρ is the dislocation density, estimated via XRD line broadening analysis in MAUD software using Equation (1).

The contribution of grain boundary hardening, ΔHV_{GB}, towards the overall hardness of the interfacial region can be estimated by the well-known Hall–Petch relationship:

$$\Delta\sigma HV_{GB} = CK_{HP}d^{-1/2} \tag{7}$$

where K_{HP} is the material-dependent Hall–Petch constant with a value of 2.8*MPa $m^{-1/2}$, taken based on the assessment in [52,55], and d is the average grain size determined from EBSD analysis.

Equations (2)–(7) are used for the linear additive model to quantitatively evaluate the individual strengthening contributions, and then they are summed to provide a predicted overall hardness value, $HV_{\text{predicted}}$, of the interfacial region. Table 4 lists all values of constants and parameters used for this model, which are attained based on the results of the present study and from those in other literature.

Table 4. Values of constants and other parameters used for calculations in the hardening model.

Hardening Mechanism	Symbol	Value	References
Solid solution	C_i	3	[56]
	M	3.05	[52]
	b	0.26 nm	[27,28,46]
	G	77,000 GPa	[52,53]
	α_1	0.3	[54]
	k_{Cr}	6.96 MPa/at. $\%^{2/3}$ Cr	[48]
	k_{Nb}	10.58 MPa/at. $\%^{2/3}$ Nb	[48]
	k_{Mo}	10.05 MPa/at. $\%^{2/3}$ Mo	[48]
	k_{Ti}	9.18 MPa/at. $\%^{2/3}$ Ti	[48]
Orowan (precipitation)	$f_{ppt.}$	1.43 vol. %	This work (TEM)
	$r_{ppt.}$	15.0 nm	This work (TEM)
Dislocation	ρ_{total}	0.942×10^{13} m^{-2}	This work (XRD)
	D_C	280 nm	This work (XRD)
Grain boundary	K_{HP}	2.8 MPa $m^{-1/2}$	[52,55]
	d	45 μm	This work (EBSD)

The overall $HV_{\text{predicted}}$ value obtained based on the modelling results is then compared with the measured average hardness value, HV_{measured}, attained via Vickers microhardness measurements taken in the interfacial region in this study. Table 5 displays these values, as well as the modelling results of the quantitative contributions of individual hardening mechanisms towards the overall $HV_{\text{predicted}}$ value. The overall predicted and measured HV values show good correspondence between each other with only a slight deviation (~3.5%), suggesting that the present modelling approach is capable of adequately estimating the interfacial hardness of the MM SLM-fabricated 316L SS/IN 718.

Table 5. Measured vs. predicted overall hardness and contribution of individual hardening mechanisms.

HV_0	HV_{SS}	HV_{ORO}	HV_ρ	HV_{GB}	$HV_{Predicted}$	$HV_{Measured}$	Error (%)
6	43	14	55	133	251	260	3.5

Based on the modelling results presented in Table 5, grain boundary hardening provides the highest contribution to the overall interfacial hardness (~53.1%). This is followed by a close competition between dislocation (55 HV, or ~21.9%) and solid solution (43 HV, or ~17.3%) hardening mechanisms. This competing role of both hardening mechanisms in the interfacial region can be attributed to the mutually high concentrations of (i) microsegregations of heavy alloying elements, particularly Nb and Ti at the boundaries of the cellular sub-structures as well as inside the matrix, and (ii) dense dislocation networks and pileups in comparison with CM metallic materials. Contrastingly, the lowest contributions of intrinsic hardness and precipitation hardening, accounting for ~0.87% and ~1.95%, respectively, could be due to the absence of any heat treatment processes in this study, since it is known that the precipitates are commonly activated for precipitation hardening after undergoing suitable heat treatment processes for alloys such as IN 718 [38].

5. Conclusions

In this study, the interfacial microstructures, hardness, and hardening mechanisms of an MM alloy combination (316L SS/IN 718) fabricated by the MM SLM process have been

investigated via EBSD, SEM, TEM, EDX, XRD, and Vickers microhardness and nanoindentation measurements. The hardening mechanisms have been evaluated based on a linear additive model, and the following conclusions can be drawn from the outcomes of this study:

1. Multi-material 316L SS/IN 718 parts with high densification levels and low porosity content (>99% and ~0.81%, respectively) have been successfully manufactured using the in-house-developed MM SLM system.
2. Nb- and Ti-rich carbides and Laves phase precipitates can be observed in the interfacial region of the MM SLM specimen based on TEM observations and EDX analysis.
3. HV and nanoindentation measurements indicate that the interfacial hardness is between that of the individual IN 718 region (highest) and that of the individual 316L SS region (lowest).
4. The hardening model built based on the linear additive theory suggests that the overall interfacial hardness is primarily provided by grain boundary hardening, followed by dislocation and solid solution hardening mechanisms. Precipitation hardening and intrinsic hardness contribute the least towards the overall interfacial hardness.

Author Contributions: Conceptualisation, S.M.Y., S.Y. and N.G.; data curation, N.M. and N.H.M.; formal analysis, S.M.Y., N.M., N.H.M., N.A.N. and S.A.M.; funding acquisition, S.M.Y.; investigation, S.M.Y., X.Z. and Y.C.; methodology, S.M.Y., X.Z. and Y.C.; project administration, S.M.Y. and N.G.; resources, S.M.Y., N.M. and N.H.M.; supervision, S.M.Y. and N.G.; validation, S.M.Y. and N.A.N.; visualisation, S.M.Y., N.M. and N.H.M.; writing—original draft, S.M.Y.; writing—review and editing, S.M.Y., S.A.M. and N.G.. All authors have read and agreed to the published version of the manuscript.

Funding: This work was supported by UTMSPACE under UTMSPACE Contract Research Grant (UTMSPC: R.K130000.7743.4J572) for this study.

Data Availability Statement: Data are unavailable as they are part of an ongoing study.

Conflicts of Interest: The authors declare no conflict of interest. The funders had no role in the design of the study; in the collection, analyses, or interpretation of data; in the writing of the manuscript; or in the decision to publish the results.

References

1. Kah, P.; Martikainen, M.S.J. Trends in Joining Dissimilar Metals by Welding. *Adv. Mater. Sport. Equip. Des.* **2014**, *440*, 269–276. [CrossRef]
2. Wei, C.; Zhang, Z.; Cheng, D.; Sun, Z.; Zhu, M.; Li, L. An overview of laser-based multiple metallic material additive manufacturing: From macro: From micro-scales. *Int. J. Extrem. Manuf.* **2021**, *3*, 012003. [CrossRef]
3. Bandyopadhyay, A.; Heer, B. Additive manufacturing of multi-material structures. *Mater. Sci. Eng. R Rep.* **2018**, *129*, 1–16. [CrossRef]
4. Chen, J.; Yang, Y.; Song, C.; Zhang, M.; Wu, S.; Wang, D. Interfacial microstructure and mechanical properties of 316L /CuSn10 multi-material bimetallic structure fabricated by selective laser melting. *Mater. Sci. Eng. A* **2019**, *752*, 75–85. [CrossRef]
5. Liu, Z.H.; Zhang, D.Q.; Sing, S.L.; Chua, C.K.; Loh, L.E. Interfacial characterization of SLM parts in multi-material processing: Metallurgical diffusion between 316L stainless steel and C18400 copper alloy. *Mater. Charact.* **2014**, *94*, 116–125. [CrossRef]
6. Chen, J.; Yang, Y.; Song, C.; Wang, D.; Wu, S.; Zhang, M. Influence mechanism of process parameters on the interfacial characterization of selective laser melting 316L/CuSn10. *Mater. Sci. Eng. A* **2020**, *792*, 139316. [CrossRef]
7. Bai, Y.; Zhang, J.; Zhao, C.; Li, C.; Wang, H. Dual interfacial characterization and property in multi-material selective laser melting of 316L stainless steel and C52400 copper alloy. *Mater. Charact.* **2020**, *167*, 110489. [CrossRef]
8. Wei, C. Multiple Material Selective Laser Melting: A New Approach. *Laser User.* **2018**, *18*, 18–19.
9. Wei, C.; Li, L.; Zhang, X.; Chueh, Y.H. 3D printing of multiple metallic materials via modified selective laser melting. *CIRP Ann.* **2018**, *67*, 245–248. [CrossRef]
10. Bodner, S.C.; van de Vorst, L.T.G.; Zalesak, J.; Todt, J.; Keckes, J.F.; Maier-Kiener, V.; Sartory, B.; Schell, N.; Hooijmans, J.W.; Saurwalt, J.J.; et al. Inconel-steel multilayers by liquid dispersed metal powder bed fusion: Microstructure, residual stress and property gradients. *Addit. Manuf.* **2020**, *32*, 101027. [CrossRef]
11. Chen, N.; Khan, H.A.; Wan, Z.; Lippert, J.; Sun, H.; Shang, S.L.; Liu, Z.K.; Li, J. Microstructural characteristics and crack formation in additively manufactured bimetal material of 316L stainless steel and Inconel 625. *Addit. Manuf.* **2020**, *32*, 101037. [CrossRef]
12. Henderson, M.B.; Arrell, D.; Larsson, R.; Heobel, M.; Marchant, G. Nickel based superalloy welding practices for industrial gas turbine applications. *Sci. Technol. Weld. Join.* **2004**, *9*, 13–21. [CrossRef]

13. Locci, I.E.; Bowman, C.L.; Gabbs, T.P.; Rd, B.; Got, I.E.L. Development of High Temperature Dissimilar Joint Technology for Fission Surface Power Systems. In Proceedings of the 4th International Brazing and Soldering Conference (IBSC), Orlando, FL, USA, 26–29 April 2009; Volume 718, pp. 165–175.
14. Ferretti, S.; Valenzano, G.; Cugno, W. International space station external active thermal control system lines manufacturing. In Proceedings of the 57th International Astronautical Congress, Valencia, Spain, 2–6 October 2006; pp. 2952–2955. [CrossRef]
15. Hinojos, A.; Mireles, J.; Reichardt, A.; Frigola, P.; Hosemann, P.; Murr, L.E.; Wicker, R.B. Joining of Inconel 718 and 316 Stainless Steel using electron beam melting additive manufacturing technology. *Mater. Des.* **2016**, *94*, 17–27. [CrossRef]
16. Wen, S.; Chen, K.; Che, Y. Tailored microstructure and robust joint of Inconel 718/316L bimetallic multi-material fabricated by selective laser melting. *Chinese J. Mech. Eng.* **2020**, preprint. [CrossRef]
17. Mei, X.; Wang, X.; Peng, Y.; Gu, H.; Zhong, G.; Yang, S. Interfacial characterization and mechanical properties of 316L stainless steel/inconel 718 manufactured by selective laser melting. *Mater. Sci. Eng. A* **2019**, *758*, 185–191. [CrossRef]
18. Mohd Yusuf, S.; Zhao, X.; Yang, S.; Gao, N. Interfacial characterisation of multi-material 316L stainless steel/Inconel 718 fabricated by laser powder bed fusion. *Mater. Lett.* **2021**, *284*, 128928. [CrossRef]
19. Lutterotti, L.; Gialanella, S. X-Ray Diffraction Characterization of Heavily Deformed Metallic Specimens. *Acta Mater.* **1998**, *46*, 101–110. [CrossRef]
20. Mccusker, L.B.; Von Dreele, R.B.; Cox, D.E.; Louër, D.; Scardi, P. Rietveld refinement guidelines. *J. Appl. Crystallogr.* **1999**, *32*, 36–50. [CrossRef]
21. Young, R.A.; Wiles, D.B. Profile Shape Functions in Rietveld Refinements. *J. Appl. Crystallogr.* **1982**, *15*, 430–438. [CrossRef]
22. Sames, W.J.; List, F.A.; Pannala, S.; Dehoff, R.R.; Babu, S.S. The metallurgy and processing science of metal additive manufacturing. *Int. Mater. Rev.* **2016**, *61*, 315–360. [CrossRef]
23. Gorsse, S.; Hutchinson, C.; Gouné, M.; Banerjee, R. Additive manufacturing of metals: A brief review of the characteristic microstructures and properties of steels, Ti-6Al-4V and high-entropy alloys. *Sci. Technol. Adv. Mater.* **2017**, *18*, 584–610. [CrossRef]
24. Tucho, W.M.; Lysne, V.H.; Austbø, H.; Sjolyst-Kverneland, A.; Hansen, V. Investigation of effects of process parameters on microstructure and hardness of SLM manufactured SS316L. *J. Alloys Compd.* **2018**, *740*, 910–925. [CrossRef]
25. Pham, M.S.; Dovgyy, B.; Hooper, P.A. Twinning induced plasticity in austenitic stainless steel 316L made by additive manufacturing. *Mater. Sci. Eng. A* **2017**, *704*, 102–111. [CrossRef]
26. Cao, G.H.; Sun, T.Y.; Wang, C.H.; Li, X.; Liu, M.; Zhang, Z.X.; Hu, P.F.; Russell, A.M.; Schneider, R.; Gerthsen, D.; et al. Investigations of γ′ γ″ and δ precipitates in heat-treated Inconel 718 alloy fabricated by selective laser melting. *Mater. Charact.* **2018**, *136*, 398–406. [CrossRef]
27. Tikhonova, M.; Enikeev, N.; Valiev, R.Z.; Belyakov, A.; Kaibyshev, R. Submicrocrystalline austenitic stainless steel processed by cold or warm high pressure torsion. *Mater. Sci. Forum.* **2016**, *838–839*, 398–403. [CrossRef]
28. De Jaeger, J.; Solas, D.; Baudin, T.; Fandeur, O.; Schmitt, J.H.; Rey, C. INCONEL 718 Single and Multipass Modelling of Hot Forging. *Superalloys* **2012**, *2012*, 663–672. [CrossRef]
29. Mohd Yusuf, S.; Chen, Y.; Yang, S.; Gao, N. Microstructural evolution and strengthening of selective laser melted 316L stainless steel processed by high-pressure torsion. *Mater. Charact.* **2020**, *159*, 110012. [CrossRef]
30. Skiba, T.; Baufeld, B.; Van der Biest, O. Shaped metal deposition of 300M steel. *Proc. Inst. Mech. Eng. Part B J. Eng. Manuf.* **2011**, *225*, 831–839. [CrossRef]
31. Amato, K.N.; Gaytan, S.M.; Murr, L.E.; Martinez, E.; Shindo, P.W.; Hernandez, J.; Collins, S.; Medina, F. Microstructures and mechanical behavior of Inconel 718 fabricated by selective laser melting. *Acta Mater.* **2012**, *60*, 2229–2239. [CrossRef]
32. Sing, S.L.; Lam, L.P.; Zhang, D.Q.; Liu, Z.H.; Chua, C.K. Interfacial characterization of SLM parts in multi-material processing: Intermetallic phase formation between AlSi10Mg and C18400 copper alloy. *Mater. Charact.* **2015**, *107*, 220–227. [CrossRef]
33. Terrazas, C.A.; Gaytan, S.M.; Rodriguez, E.; Espalin, D.; Murr, L.E.; Medina, F.; Wicker, R.B. Multi-material metallic structure fabrication using electron beam melting. *Int. J. Adv. Manuf. Technol.* **2013**, *71*, 33–45. [CrossRef]
34. Gu, D.D.; Meiners, W.; Wissenbach, K.; Poprawe, R. Laser additive manufacturing of metallic components: Materials, processes and mechanisms. *Int. Mater. Rev.* **2012**, *57*, 133–164. [CrossRef]
35. Deng, D.; Peng, R.L.; Brodin, H.; Moverare, J. Microstructure and mechanical properties of Inconel 718 produced by selective laser melting: Sample orientation dependence and effects of post heat treatments. *Mater. Sci. Eng. A* **2018**, *713*, 294–306. [CrossRef]
36. Kuo, Y.L.; Horikawa, S.; Kakehi, K. The effect of interdendritic δ phase on the mechanical properties of Alloy 718 built up by additive manufacturing. *Mater. Des.* **2017**, *116*, 411–418. [CrossRef]
37. Tucho, W.M.; Cuvillier, P.; Sjolyst-Kverneland, A.; Hansen, V. Microstructure and hardness studies of Inconel 718 manufactured by selective laser melting before and after solution heat treatment. *Mater. Sci. Eng. A* **2017**, *689*, 220–232. [CrossRef]
38. Chlebus, E.; Gruber, K.; Kuźnicka, B.; Kurzac, J.; Kurzynowski, T. Effect of heat treatment on the microstructure and mechanical properties of Inconel 718 processed by selective laser melting. *Mater. Sci. Eng. A* **2015**, *639*, 647–655. [CrossRef]
39. Antonsson, T.; Fredriksson, H. Effect of cooling rate on the solidification of INCONEL 718. *Metall. Mater. Trans. B* **2005**, *36B*, 85–96. [CrossRef]
40. Knorovsky, G.A.; Cieslak, M.J.; Headley, T.J.; Romig, A.D.; Hammetter, W.F. INCONEL 718: A solidification diagram. *Metall. Trans. A* **1989**, *20*, 2149–2158. [CrossRef]

41. Devendranath Ramkumar, K.; Patel, S.D.; Sri Praveen, S.; Choudhury, D.J.; Prabaharan, P.; Arivazhagan, N.; Xavior, M. A Influence of filler metals and welding techniques on the structure-property relationships of Inconel 718 and AISI 316L dissimilar weldments. *Mater. Des.* **2014**, *62*, 175–188. [CrossRef]
42. Bansal, A.; Sharma, A.K.; Das, S.; Kumar, P. On microstructure and strength properties of microwave welded Inconel 718/stainless steel (SS-316L). *Proc. Inst. Mech. Eng. Part L J. Mater. Des. Appl.* **2016**, *230*, 939–948. [CrossRef]
43. Li, Y.F.; Hong, S.T.; Choi, H.; Han, H.N. Solid-state dissimilar joining of stainless steel 316L and Inconel 718 alloys by electrically assisted pressure joining. *Mater. Charact.* **2019**, *154*, 161–168. [CrossRef]
44. Morris, D.G. Strengthening mechanisms in nanocrystalline metals. In *Nanostructured Metals and Alloys Processing, Microstructure, Mechanical Properties and Applications*; Woodhead Publishing Co.: Delhi, India, 2011; pp. 299–328. [CrossRef]
45. Zhang, P.; Li, S.X.; Zhang, Z.F. General relationship between strength and hardness. *Mater. Sci. Eng. A* **2011**, *529*, 62–73. [CrossRef]
46. Asadi, M.; Guillot, D.; Weck, A.; Hegde, S.R.; Koul, A.K.; Sawatzky, T.; Saari, H. Constructing a validated deformation mechanisms map using low temperature creep strain accommodation processes for nickel-base alloy 718. *Am. Soc. Mech. Eng. Press. Vessel. Pip. Div. PVP* **2012**, *2*, 65–73. [CrossRef]
47. Lasalmonie, A.; Strudel, J.L. Influence of grain size on the mechanical behaviour of some high strength materials. *J. Mater. Sci.* **1986**, *21*, 1837–1852. [CrossRef]
48. Goodfellow, A.J. Strengthening mechanisms in polycrystalline nickel-based superalloys. *Mater. Sci. Technol.* **2018**, *34*, 1793–1808. [CrossRef]
49. Gladman, T. Precipitation-hardening of metals. *Mater. Sci. Technol.* **1999**, *15*, 30–36. [CrossRef]
50. Hadadzadeh, A.; Amirkhiz, B.S.; Mohammadi, M. Contribution of Mg2Si precipitates to the strength of direct metal laser sintered AlSi10Mg. *Mater. Sci. Eng. A* **2019**, *739*, 295–300. [CrossRef]
51. Chen, B.; Moon, S.K.; Yao, X.; Bi, G.; Shen, J.; Umeda, J.; Kondoh, K. Strength and strain hardening of a selective laser melted AlSi10Mg alloy. *Scr. Mater.* **2017**, *141*, 45–49. [CrossRef]
52. Karavaeva, M.V.; Abramova, M.M.; Enikeev, N.A.; Raab, G.I.; Valiev, R.Z. Superior strength of austenitic steel produced by combined processing, including equal-channel angular pressing and rolling. *Metals* **2016**, *6*, 310. [CrossRef]
53. Maher.Com. Alloy 718 Data Sheet. 2016. Available online: https://www.maher.com/media/pdfs/718-datasheet.pdf (accessed on 10 December 2019).
54. Kim, J.G.; Enikeev, N.A.; Seol, J.B.; Abramova, M.M.; Karavaeva, M.V.; Valiev, R.Z.; Park, C.G.; Kim, H.S. Superior Strength and Multiple Strengthening Mechanisms in Nanocrystalline TWIP Steel. *Sci. Rep.* **2018**, *8*, 11200. [CrossRef] [PubMed]
55. Gubicza, J.; El-Tahawy, M.; Huang, Y.; Choi, H.; Choe, H.; Lábár, J.L.; Langdon, T.G. Microstructure, phase composition and hardness evolution in 316L stainless steel processed by high-pressure torsion. *Mater. Sci. Eng. A* **2016**, *657*, 215–223. [CrossRef]
56. Li Ning, J.; Courtois-Manara, E.; Kurmanaeva, L.; Ganeev, A.V.; Valiev, R.Z.; Kübel, C.; Ivanisenko, Y. Tensile properties and work hardening behaviors of ultrafine grained carbon steel and pure iron processed by warm high pressure torsion. *Mater. Sci. Eng. A* **2013**, *581*, 8–15. [CrossRef]